Structure and recombination in InGaAs/GaAs heterostructures

E. A. Fitzgerald, D. G. Ast, P. D. Kirchner, G. D. Pettit, and J. M. Woodall

Structure and recombination in InGaAs/GaAs heterostructures

E. A. Fitzgerald and D. G. Ast
Department of Materials Science and Engineering, Cornell University, Ithaca, New York 14853

P. D. Kirchner, G. D. Pettit, and J. M. Woodall
IBM T. J. Watson Research Center, Yorktown Heights, New York 10598

The defect structure of lattice-mismatched 1-μm In$_x$Ga$_{1-x}$As ($x \approx 0.12$, misfit $\Delta a/a \approx 8.5 \times 10^{-3}$) epilayers on GaAs was studied with scanning cathodoluminescence (CL), transmission electron microscopy (TEM), high-voltage electron microscopy, and scanning electron microscopy. CL shows that nonradiative recombination lines exist in the GaAs buffer layer as far as 4000 Å from the interface. The density of these defects is independent of substrate dislocation density. Plan-view TEM analysis indicates that the majority of these dislocations in the buffer layer are sessile edge half-loops. Cross-sectional TEM shows that loops also extend into the InGaAs epilayer, but the majority of the loops are located on the buffer layer (substrate) side of the interface. A model is proposed to explain sessile edge dislocation formation in the buffer layer. A comparison of CL and high-voltage electron microscopy images from the same interface area reveals that the dark nonradiative recombination lines seen in scanning luminescence images in this high misfit system do not correspond to the normal, isolated misfit dislocation. The nonradiative recombination line spacing is 3 μm, whereas the interface dislocation spacing is 400–1000 Å. It is shown that the nonradiative recombination lines observed in CL of the interface correspond to specific groups of dislocations with different TEM contrast behavior. The dark nonradiative recombination lines also correlate with asymmetric surface ridges, suggesting that they introduce preferred nucleation sites, and that these effects are different for the two ⟨110⟩ directions.

I. INTRODUCTION

Many devices employing heterojunctions are based upon the Al$_x$Ga$_{1-x}$As/GaAs heterojunction. However, deep levels in Al$_x$Ga$_{1-x}$As limit device performance.[1,2] One alternative system is the In$_x$Ga$_{1-x}$As/GaAs system. Devices using this heterojunction include solar cells,[3] high electron mobility transistors,[4] and heterojunction bipolar transistors.[5,6]

The major problem in the InGaAs/GaAs system is that the lattice mismatch between the InGaAs and GaAs layers creates defects at the interface. For single In$_x$Ga$_{1-x}$As epilayers on GaAs the strain can be accommodated elastically if the thickness of the In$_x$Ga$_{1-x}$As is less than the critical thickness for defect formation,[7] which depends upon the In concentration in the epilayer. However, many potential uses require higher In concentrations and/or epilayers thicker than the critical thickness. Under such conditions, misfit dislocations will form.

Photoluminescence and electroluminescence have been used in previous studies of degraded lasers[8,9] and other devices[10] to correlate the electrical activity of defects with their structure as seen in transmission electron microscopy (TEM). However, photoluminescence and electroluminescence usually lack the resolution of electron beam excitation techniques such as cathodoluminescence (CL) and electron-beam-induced current. Petroff, Logan, and Savage[11] have demonstrated the effectiveness of CL and electron-beam-induced current in the scanning transmission electron microscope by investigating the nonradiative recombination at individual misfit dislocations between Ga$_{1-x}$Al$_x$As$_{1-y}$P$_y$ epilayers.

In this paper, we report new findings in the structure and recombination at the InGaAs/GaAs interface. We have used CL in the scanning electron microscope (SEM), TEM, high-voltage electron microscopy (HVEM), and secondary electron imaging to correlate recombination, surface morphology, and defect structure.

II. EXPERIMENTAL PROCEDURE

To check for the influence of the substrate dislocation density on interface morphology, epilayers were deposited on GaAs substrates with two dislocation densities: 9800 cm^{-2} and < 100 cm^{-2} as determined by etch pit density. The CL measurement of the substrate dislocation density was 6000–7000 cm^{-2} and < 100 cm^{-2}. 1-μm-thick GaAs buffer layers were grown by molecular-beam epitaxy on each substrate, followed by a layer of In$_x$Ga$_{1-x}$As with a uniform In concentration, varying x from 0.11 to 0.15. The epilayer thickness varied from 1 to 1.3 μm. The growth temperature was 550 °C, and the growth rate was 1 μm/h. All layers grown were silicon doped at 10^{18} cm^{-3} for two reasons: films doped at 10^{17}–10^{18} cm^{-3} are technologically important in device structures, and the luminescence efficiency is optimum at $\approx 10^{18}$ cm^{-3}, thus improving the CL signal. The epilayer thickness was measured with Rutherford backscattering spectrometry and cross-sectional TEM, and the composition was determined with Rutherford backscattering spectrometry and wavelength sensitive CL.

The heterostructures were analyzed with two types of CL systems, which were installed in a JEOL JSM 35C SEM. The system used to produce CL images was an annular sili-

con *p-i-n* detector mounted under the pole piece of the microscope and approximately 15 mm from the sample.[12] The detector was sensitive to a range of wavelengths (≈ 0.55–1.05 μm) and therefore detected both InGaAs and GaAs radiation emitted from the sample. The large solid angle of this detector resulted in a high collection efficiency. Therefore, detailed images could be obtained at voltages as low as 15 keV. At this accelerating voltage, beam damage to the sample is eliminated, and the resolution limit is approximately 1–2 μm.

The other CL system used was a wavelength-sensitive system to determine whether the images originated from the InGaAs epilayer or the GaAs buffer layer. A fiber optic bundle was placed in close proximity (≈ 3 mm) to the sample in the SEM. The light collected was guided by the bundle through the SEM chamber wall to a single lens collimator. The collimated light then passed into a grating monochromator, and an infrared photomultiplier tube was positioned at the exit slit to detect the radiation. The amplified photomultiplier signal was plotted versus wavelength.

In addition to these two CL systems, the SEM is equipped for energy dispersive x-ray analysis (EDX) and backscattered electron imaging. The backscatter electron detector is an annular detector similar to the CL detector. The annular CL detector can be withdrawn from the pole piece to expose the backscattered electron detector in order to obtain CL and backscattered electron signals from the same area.

To investigate the depth variation of the defects, step-etched specimens with stairlike profiles were fabricated by repeatedly masking with wax and etching with a H_3PO_4:H_2O_2:DI H_2O 3:1:50 mixture. Step heights were measured with both a stylus profile apparatus and an interference microscope. Rutherford backscattering spectrometry and EDX were used in addition to wavelength sensitive CL to verify that the steps etched through the InGaAs overlayer were free of In.

Planar TEM samples were prepared by first etching off the top ≈ 8000 Å of the epilayer by using the above etching solution. To obtain a sample that is transparent to electrons at the interface, it is desirable to remove as much material above the interface as possible. However, a good CL signal requires a thicker sample; therefore, ≈ 2000 Å of InGaAs was left above the interface. From the opposite (substrate) side, material was then removed by a chemical jet with the use of a H_2SO_4:H_2O_2:DI H_2O 5:1:1 solution. Cross-sectional TEM samples were prepared by gluing a support piece of GaAs with epoxy to the epilayer surface. Samples were then cut perpendicular to the original sample surface along the (110) planes, polished, and finally thinned with Ar-ion milling.

TEM was performed on both planar and cross-sectional samples in the JEOL 200 CX scanning transmission electron microscope. For the HVEM/CL correlation, a thick specimen without a hole was examined. After obtaining CL images of the sample, we used the 1.2-MeV HVEM at the New York State HVEM facility in Albany, NY to produce excellent low-magnification images of thick specimens for correlation with CL images.

III. RESULTS AND DISCUSSION

A. CL and SEM analysis of step-etched specimens

Figures 1(a)–1(d) are CL images and corresponding CL spectra of a step-etched 1-μm $In_{0.12}Ga_{0.88}As$ epilayer grown on a substrate with < 100 dislocations cm^{-2}. The etch profile of the sample was stairlike, consisting of ≈ 2000-Å steps. Each CL image is from a single step. All CL images were taken at the same magnification with the electron beam perpendicular to the plane of the heterojunction. The beam voltage was 15 kV, and the specimen current was 40 nA. In Figs. 1(a) and 1(b), the steps are located 1 μm (unetched) and 5000 Å above the interface, respectively. Figures 1(c) and 1(d) show images of steps etched to the interface and 1000 Å below the interface, respectively. CL images from a buffer layer grown in the same run, without an InGaAs overlayer, show ≈ 6000 threading dislocations cm^{-2} appearing as black spots in an otherwise homogeneous background intensity.

The CL spectrum of the unetched InGaAs (1-μm) layer consists mostly of InGaAs radiation. The 15-keV electron range in GaAs is approximately 1.6 μm, but most of the higher-energy GaAs photons created below the heterojunction are absorbed in the smaller band-gap InGaAs layer and reemitted as InGaAs radiation. For the 5000-Å step, the InGaAs emission peak decreases, and the GaAs peak increases, as expected, since some of the GaAs radiation can now escape without being absorbed by the top InGaAs layer. Because the epilayer and interface are still present in these steps and because the signal originates from both the GaAs and InGaAs regions, the CL images of these steps are dominated by defects in the interface region. The decrease in total CL intensity (GaAs and InGaAs) in comparing the spectrum from Fig. 1(a) to that in 1(b) is due to the presence of high nonradiative recombination at the interface.

For CL spectra from 1(c), no InGaAs peak was observed, showing that CL images from this step originate in the GaAs buffer layer. EDX and backscattered electron imaging were used to verify the absence of InGaAs in these steps. Because the backscattered signal is proportional to the atomic number squared, a large decrease in backscattered electron signal between 1(b) and 1(c) indicates a decrease in In concentration at this step. Using the initial epilayer thickness as determined by Rutherford backscattering spectrometry and step height measurements from interference microscopy, we conclude that step 1(c) is located approximately at the interface depth. If a thin layer of InGaAs is still present, very little CL signal will originate from any thin InGaAs layer (as indicated by the spectrum), because the surface is depleted of carriers to a depth of ≈ 300 Å. Therefore, Fig. 1(c) shows the nonradiative recombination centers in the buffer layer. EDX, spectral CL, backscattered electron imaging, and Rutherford backscattering spectrometry confirm that all subsequent steps below that shown in Fig. 1(c) do not contain In and are located below the interface. A decrease in the GaAs peak intensity can be observed in the CL spectra from 1(d), indicating that part of the electron beam excitation volume is in the lower doped substrate, where luminescence is much lower. Figure 1(d) also reveals
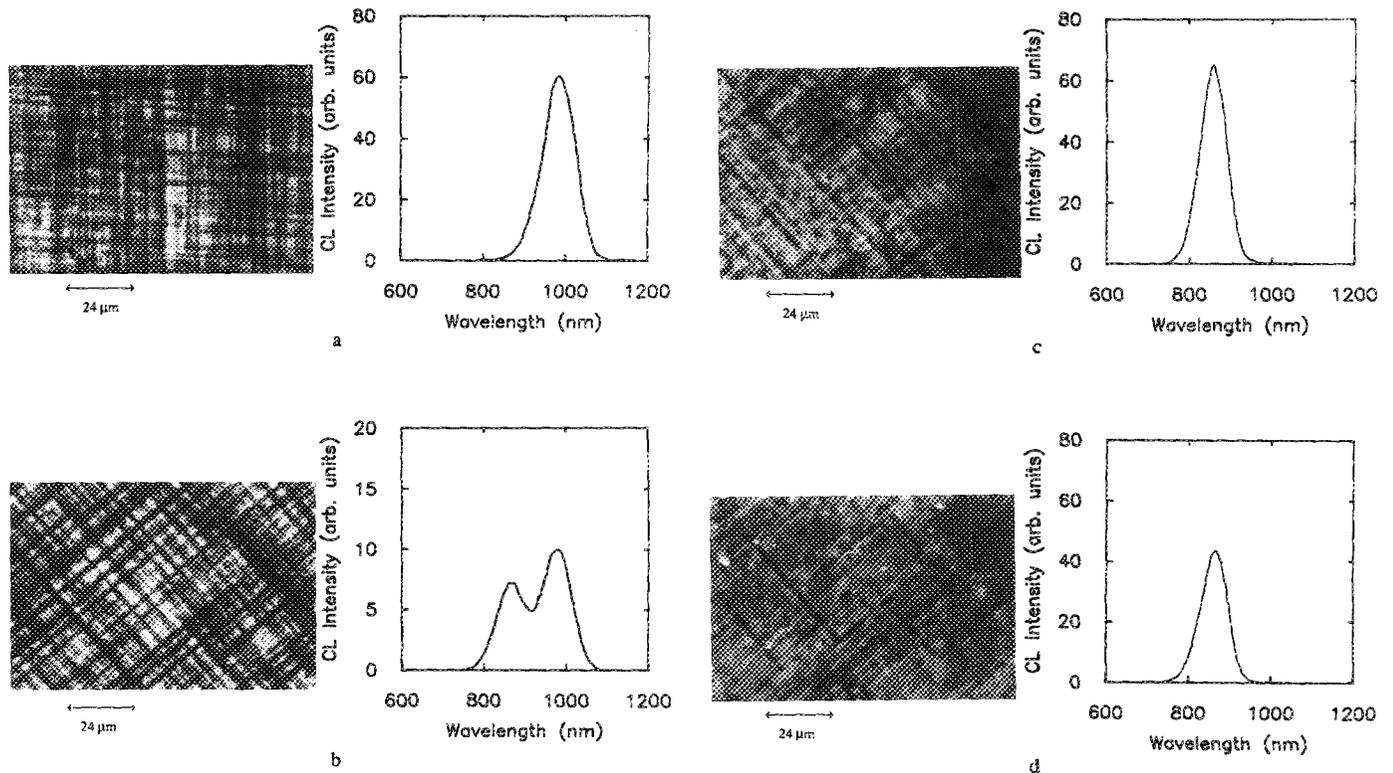
   Fitzgerald *et al.*   694

FIG. 1. Plan-view 15-keV CL images and their corresponding spectra of the $In_{0.12}Ga_{0.88}As/GaAs$ step-etched sample; (a) 1 μm above the interface; (b) 5000 Å above the interface; (c) interface region; (d) $\approx$ 1000 Å below the interface.

that the defects in the buffer layer are strong nonradiative recombination centers. The rest of the step-etched sample shows that the nonradiative recombination centers are present as far as 4000 Å into the buffer layer, and their density decreases with distance from the interface.

The InGaAs epilayers grown on high dislocation density substrates (9800 cm^{-2}) were analyzed by using the same methods and produced identical results. Both samples show a buffer layer defect density of $\approx 10^6 cm^{-2}$ at ≈ 1000 Å below the interface. Therefore, the concentration of defects in the buffer layer is independent of substrate dislocation density. We conclude that these defects were not produced by threading dislocations from the substrate; i.e., they must be a product of the mismatched interface. All evidence indicates that nonradiative recombination occurs at defects in the buffer layer, and that this effect is independent of substrate dislocation density.

B. TEM analysis of buffer layer defects

To investigate the defects responsible for high nonradiative recombination in the buffer layer, we first prepared TEM stereomicrographs using the samples with 1-μm $In_{0.12}Ga_{0.88}As$ epilayers. Figures 2(a) and 2(b) are stereomicrographs taken under the same $\langle 220 \rangle$ two-beam condition on opposite sides of the [001] pole. The total tilt between pictures is 10°. The pictures are oriented so that the three-dimensional view is from the buffer layer side of the interface. Two large, inclined, looping dislocations in the buffer layer are easily visible, as well as some smaller loops.

Note that the buffer layer dislocation ends are pinned down at the interface, most likely a result of a reaction with an interface dislocation. Also, the buffer layer dislocations are emanating from an area of high interface dislocation density, indicating that increased local stress at the interface plays an important role in this process. Looping dislocations were seen infrequently on the epilayer (InGaAs) side of the interface.

To more accurately determine the distribution of looping above and below the interface, we have also prepared
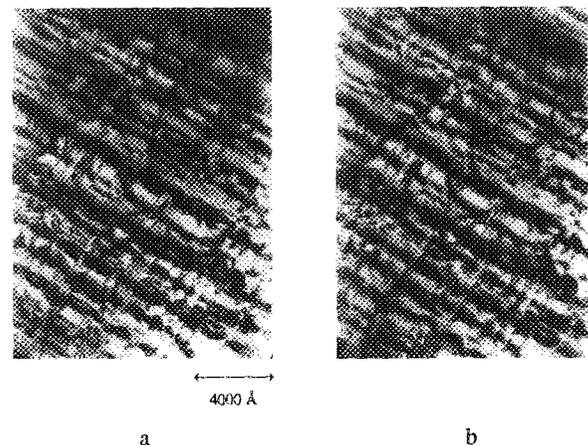

FIG. 2. Stereo TEM micrographs of the dislocations looping away from the interface. The micrographs are arranged so that the view is from the GaAs buffer layer side of the heterojunction.

cross-sectional TEM specimens. Figure 3(a) shows looping dislocations in the buffer layer, but relatively few in the InGaAs overlayer. In fact, this was a general trend seen in cross-sectional samples, confirming the results from the above stereopairs.

We also note that the depths to which the loops penetrate agree with the estimates from the step-etched CL measurements. Recall that CL measures the farthest propagation from the interface to be 3000–4000 Å, with the majority lying within 2000 Å. In the TEM micrograph shown in Fig. 3(a), the loops reach $\approx$ 820, 2050, 1400, and 3000 Å below the interface, agreeing with the CL results. Figure 3(b) is a higher magnification micrograph showing a few loops at the interface more clearly.

To investigate the crystallographic nature of these defects, the epilayer and interface were removed by chemical etching, leaving the buffer layer. CL images from these specimens were similar to Fig. 1(d), which shows a step clearly below the interface. The samples were then thinned from the substrate side and analyzed with a 200-keV TEM.
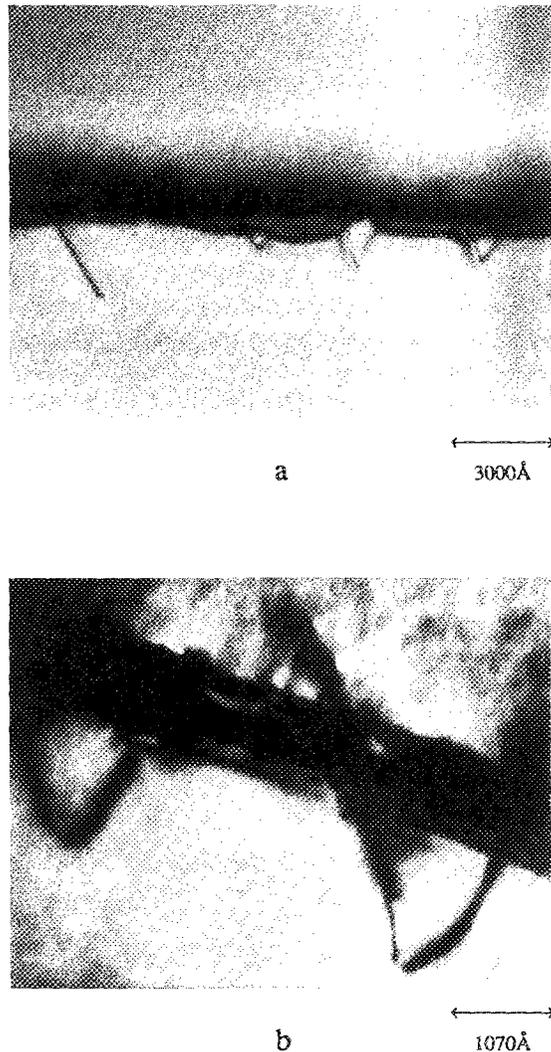
Figures 4(a)–4(c) are a series of micrographs used for Burgers vector analysis of the dislocations in the sample, and Fig. 4(d) is a micrograph of another sample revealing the density of buffer layer defects closer to the interface. All dislocations in Fig. 4, especially those denoted by 1 and 2, show areas along the dislocation line which are periodically pinned or restricted. Dislocation interactions at the interface or sessile dislocations can hinder or prevent dislocations from gliding away from the interface, thus forming restrictive nodes at these junctions [also seen in Figs. 2(a) and 2(b)]. Note dislocation 3 to the right-hand side in Figs. 4(a)–4(c). This dislocation is being pinned down by the small looping dislocation 4. As will now be demonstrated, 4 is an edge type dislocation, and 3 is a 60° type dislocation.

Figures 4(a), 4(b), and 4(c) are two-beam bright-field micrographs of the same area with the use of g_{040}, g_{220}, and $g_{2\bar{2}0}$ reflections, respectively. As can be seen in Fig. 4(a), all the dislocations in this area are visible under g_{040} excitation. Note that dislocations 1, 2, and 3 all show strong contrast. Figure 4(b) shows that dislocation lines like 2 that are parallel to [220] disappear under g_{220} excitation. As might be expected for the other direction, dislocation 1 disappears with a $g_{2\bar{2}0}$ two-beam condition, i.e., when the g vector is parallel to the dislocation line.

The Burgers vectors for these dislocations can be determined, because dislocations lose contrast when g is perpendicular to the Burgers vector (b). This follows from the $g \cdot b$ criterion for minimum contrast at a dislocation. However, since there is no residual contrast, $g \cdot b \times u$ must also be zero, where u is a unit vector along the dislocation line. In the sphalerite crystal slip system $\langle 110 \rangle \{111\}$, the three most likely edge dislocations have a Burgers vector of $a/6\langle 112 \rangle$, $a/2\langle 110 \rangle$, or $a/6\langle 110 \rangle$. No stacking fault contrast was ob-

a   3000Å

b   1070Å

FIG. 3. Cross-sectional TEM micrographs of the $In_{0.12}Ga_{0.88}As$/GaAs interface; (a) a micrograph showing many loops on the buffer layer side of the junction; (b) a higher magnification of two buffer layer loops.

a   1 μm   b   1 μm
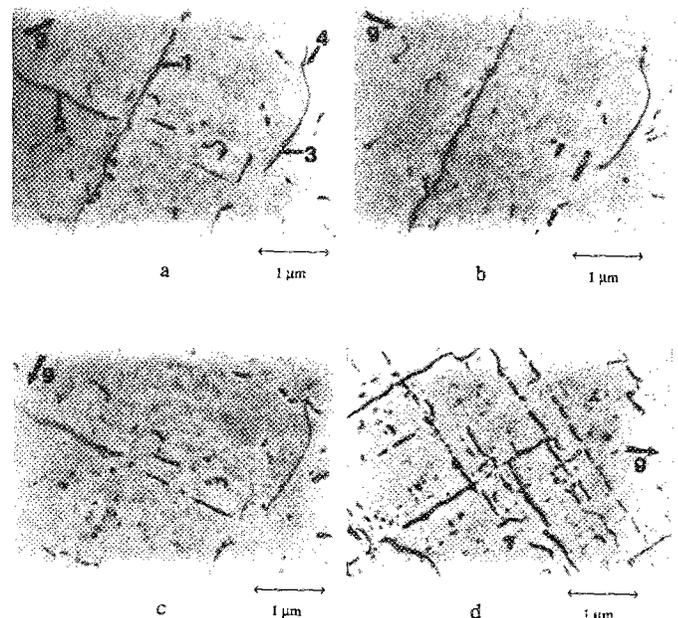
c   1 μm   d   1 μm

FIG. 4. Plan-view TEM micrographs of the buffer layer defects with the epilayer and interface removed; (a) g_{040} excitation; (b) g_{220}; (c) $g_{2\bar{2}0}$; (d) g_{040} excitation of a sample etched closer to the interface.

served, ruling out $b = a/6\langle 112 \rangle$. Therefore, dislocations of type 1 which lie along $[\bar{1}10]$ in Fig. 4 are edge dislocations with b along $[110]$. Dislocation type 2, which lies along $[110]$, has b along $[\bar{1}10]$. Sessile edge dislocations like 1 and 2 most likely result from the reaction of two glissile 60° dislocations with Burgers vectors in the same $\{111\}$ glide plane. For example,

$$\frac{a}{2}[011] + \frac{a}{2}[\bar{1}0\bar{1}] \rightarrow \frac{a}{2}[\bar{1}10]. \qquad (1)$$

If the 60° dislocations are dissociated, the 30° partials first react to form a stair rod dislocation, leaving two edge partials:

$$\frac{a}{2}[011] + \frac{a}{2}[\bar{1}0\bar{1}]$$

$$\rightarrow \frac{a}{6}[121] + \frac{a}{6}[\bar{1}12] + \frac{a}{6}[\bar{2}\bar{1}\bar{1}] + \frac{a}{6}[\bar{1}1\bar{2}], \qquad (2)$$

$$\frac{a}{6}[121] + \frac{a}{6}[\bar{1}12] + \frac{a}{6}[\bar{2}\bar{1}\bar{1}] + \frac{a}{6}[\bar{1}1\bar{2}]$$

$$\rightarrow \frac{a}{6}[\bar{1}10] + \frac{a}{6}[\bar{1}1\bar{2}] + \frac{a}{6}[\bar{1}12], \qquad (3)$$

which could contract to form the perfect sessile edge dislocation of Eq. (1):

$$\frac{a}{6}[\bar{1}10] + \frac{a}{6}[\bar{1}1\bar{2}] + \frac{a}{6}[\bar{1}12] \rightarrow \frac{a}{2}[\bar{1}10]. \qquad (4)$$

Because the stair rod and perfect edge dislocations are sessile, generation of an edge dislocation away from the interface requires two 60° dislocations to react at that distance from the interface. Once the edge dislocation is formed, it cannot move by glide.

Gliding 60° dislocations in this system are slightly dissociated,[13] and the formation of edge dislocations in the buffer layer [see Eq. (3)] depends on the sequence of partials. In a film in compression, as in the case of InGaAs on GaAs, the trailing partial, which is closest to the epilayer surface is the 90° edge partial; the leading partial is the 30° partial.[13] Therefore, the process in Eq. (3) can occur in which the two leading 30° partials react in the buffer layer. In a tensile epilayer, the leading partials are edge partials, and the 30° partials are closer to the surface. In this case, dislocations gliding in towards the substrate would have trailing 30° dislocations. Reaction (3) would then not occur. Instead of the leading 30° dislocations forming a stair rod dislocation, the leading 90° partials would form an edge dislocation with $b = a/3[\bar{1}10]$.

Although the majority of dislocations disappear under one of the two $\langle 220 \rangle$ reflections, as discussed above, a small number of dislocations like 3 in Fig. 4 retain contrast under both $\langle 220 \rangle$ two-beam conditions shown. The contrast is different for the two perpendicular $\langle 220 \rangle$ excitations. Under g_{400} excitation, dislocation 3 loses much contrast. Residual contrast with $\langle 400 \rangle$ excitation is typical of 60° dislocations.[14,15] This residual contrast is due to the fact that $g \cdot b \times u$ is not zero for the 60° dislocation when $g \cdot b = 0$. Also, the contrast of the 60° dislocation will be different for g_{220} and $g_{2\bar{2}0}$ excitations because of $g \cdot b \times u \neq 0$ when g is perpendicular to the dislocation line. This contrast behavior is observed

for dislocations of type 3 [see Figs. 4(b) and 4(c)]. We conclude that dislocation 3 is a 60° dislocation. Because 60° dislocations can be observed away from the interface, it is reasonable that 60° dislocations react away from the interface to form edge dislocations.

The pinning of dislocation 3 by dislocation 4 in Fig. 4 is one mechanism that can explain the edge dislocation segments that are confined closer to the interface. Sessile edge dislocations are known to be barriers to gliding dislocations. This pinning mechanism appears to be an important process in the formation of the edge dislocations in the buffer layer.

Because our CL results show that defects in the buffer layer appear as nonradiative recombination lines in a broken line configuration, and our TEM results show that the majority of dislocations in the buffer layer are edge dislocations with the same configuration, we conclude that the dislocations responsible for the nonradiative recombination in the buffer layer are edge dislocations. These edge dislocations are either perfect $a/2[\bar{1}10]$ type or are composed of two edge partials and a stair rod dislocation. Petroff et al.[11] found in GaAlAsP heterostructures that clean, straight, sessile edge dislocations do not act as nonradiative recombination centers. They assumed that a reconstruction of the core occurs [Eq. (4)] and a perfect edge dislocation is favored. However, our results indicate that sessile edge dislocations in the buffer layer act as nonradiative recombination centers. Thus the buffer layer dislocations are either dissociated, or if they are perfect edge dislocations, nonradiative recombination must be enhanced by the presence of kinks and jogs. The edge dislocations observed in our experiments are not entirely straight, and therefore must contain kinks and jogs along the dislocation line which are likely to be responsible for the nonradiative recombination at these dislocations.

C. HVEM/CL correlation

Figures 2(a) and 2(b) clearly show a dislocation spacing at the interface of 400–1000 Å, whereas the CL images in Figs. 1(a) and 1(b), taken from the same material, show dark nonradiative recombination lines spaced at an average distance of 3 μm. The dark nonradiative recombination lines seen by luminescence techniques from high dislocation density interfaces are therefore not associated with the majority of isolated misfit dislocations at the interface. To identify the crystallographic nature of the dark nonradiative recombination lines, we have compared CL and TEM images from the same area.

Because optimum CL images require a sample with a thickness comparable to the maximum depth of the CL signal (≈ 1–1.5 μm) and TEM images require thin samples (< 0.5 μm), an intermediate thickness must be used to obtain CL and TEM images from the same area. HVEM was used to allow the thickest samples possible for TEM (≈ 0.8–1 μm). Samples for this correlation were thinned, as described above, but etching was halted before the formation of a hole. CL images were then obtained with 15-keV electrons by using the annular CL detector. One advantage of performing CL in the SEM rather than a TEM[11] is that no damage occurs to the specimen at a 15-keV accelerating vol-

tage. Therefore, CL images could be taken from the same area several times without degradation of the sample.

We have observed that 200-keV electrons, and to a much larger extent 1-MeV electrons, do decrease the CL intensity from the sample. At typical TEM operating conditions, 200-keV electrons cause a large decrease in CL intensity after a few hours of exposure, and 1-MeV radiation destroys the CL intensity almost instantaneously. However, under our observation conditions, we did not observe any change in the geometry of line defects due to either the 200-keV or 1-MeV electrons; i.e., the interface defect morphology was not altered, indicating that TEM and HVEM are appropriate techniques for studying the structure of these interfaces.

After mapping areas on the specimen with CL, the identical areas were analyzed with a 1.2-MeV HVEM. Figure 5 is a planar CL map of an area on a specimen prepared from the 1-μm $In_{0.12}Ga_{0.88}As$ material. The symbol m denotes a particle serving as a reference marker, and dark nonradiative recombination lines are indicated by A, B, D, E, F, and G. The CL image shows a resolution of 1–2 μm. Because the majority of the CL generated by 15-keV electrons comes from a depth of 1–1.5 μm, and the sample is thinner than 1.5 μm, we expect that the excitation volume is limited by the sample thickness, ≈ 0.8 μm. The resolution in bulk samples is usually determined by the size of the excitation volume. Our CL resolution is approximately 1–2 μm. Therefore, it appears that the CL resolution is limited by the diffusion lengths of the generated carriers, rather than the size of the generation volume.

Figure 6 is a 1-MeV HVEM map of the area along line defects A, B, and C under g_{220} excitation. Note that good contrast can only be achieved in the vicinity of the g_{220} bend contour. To generate the map, the sample was tilted, and the bend contour was moved along A, B, and C. A comparison of Figs. 5 and 6 shows the correlation of A and B; however, there is no dark nonradiative recombination line in Fig. 5 corresponding to C in Fig. 6. The defects corresponding to the nonradiative recombination lines A and B are strongly
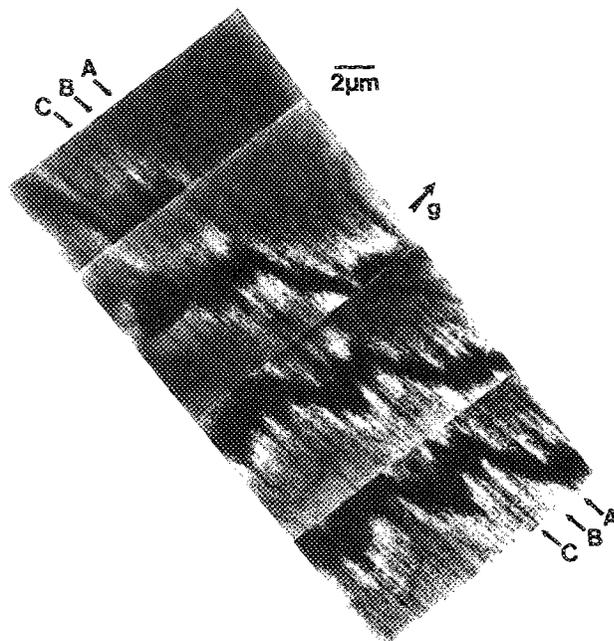

FIG. 6. 1-MeV HVEM map under g_{220} excitation from the same area as Fig. 5.

excited by g_{220} excitation, i.e., when g is perpendicular to the dislocation line. Strong contrast from C is also observed when g is perpendicular to the dislocation line. It can be seen in Fig. 6 that the defects A and B are composed of more than one misfit dislocation. Also, the bend contours shift a considerable amount when crossing over defects A, B, and C, indicating a change in thickness, a large strain field, or a combination of the two.

A 1-MeV HVEM map for $g_{2\bar{2}0}$ is shown in Fig. 7. The area is the same region as shown in Figs. 5 and 6. Defects D and E in Fig. 7 correspond to the CL nonradiative recombination lines seen in Fig. 5. Because of sample geometry, it was difficult to excite defects along [110] (like D and E) in this area, and therefore their contrast is not as good as the contrast from A, B, and C.
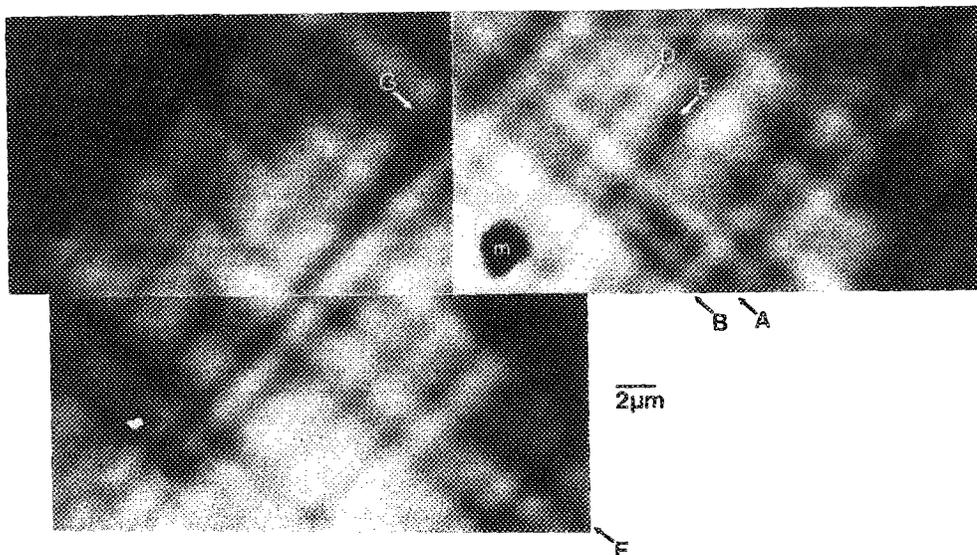

FIG. 5. High-resolution plan-view 15-keV CL map of the $In_{0.12}Ga_{0.88}As/GaAs$ interface.

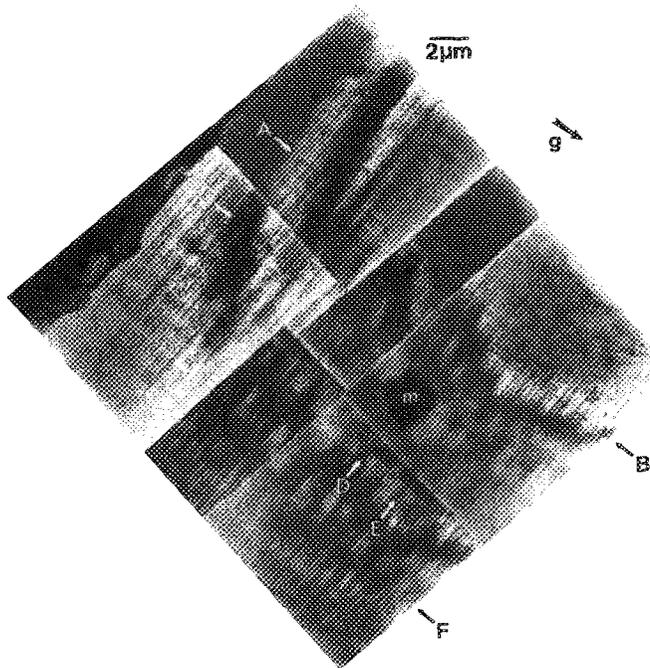FIG. 7. 1-MeV HVEM map of the same area as Figs. 5 and 6, under $g_{2\bar{2}0}$ excitation.

a   3250Å

b   3250Å

FIG. 8. Higher magnification of CL and TEM defect B; (a) g_{220} excitation; (b) $g_{2\bar{2}0}$.

Figures 6 and 7 indicate that most interface dislocation lines perpendicular to g are strongly excited, and less excited when g is parallel to the dislocation line. The defect lines A, B, and G exhibit a different contrast behavior. When g is parallel to these defects corresponding to dark nonradiative recombination lines, A, B, and G, very strong contrast still exists, as seen in Fig. 7. This is especially evident for B, which lies in the vicinity of the bend contour in Fig. 7. Other defects corresponding to nonradiative recombination lines, such as that labeled F, show the same behavior as A, B, and G.

To gain more information about the structure of the dark nonradiative recombination lines, we observed defect area B under higher magnification with 200-keV electrons. We were unable to obtain sufficient transmission in the vicinity of the [220] and [2̄20] bend contours. Figure 8(a) is a higher magnification of defect area B in Fig. 6. Under a g_{220} two-beam condition, three groups of line defects in B, marked by arrows, show extremely high contrast, higher than the other interface dislocations. The B dislocations are not straight and loop slightly away from the interface. This same area under $g_{2\bar{2}0}$ excitation is shown in Fig. 8(b). The contrast from the defects in B decreases, but the dislocations definitely do not satisfy the $g\cdot b = 0$ criterion for no contrast or minimum contrast. Recall that these same contrast features can be seen for the strongly excited defects A, F, and G in Figs. 6 and 7. Although difficult to observe, the defects in B seem to remain in contrast under g_{040} and g_{400} excitation (not shown here).

In comparison to defects like B, consider the dislocations in the rest of the interface array as seen in Figs. 8(a) and 8(b). The majority of misfit dislocations do show greater contrast when g is perpendicular to the line direction.
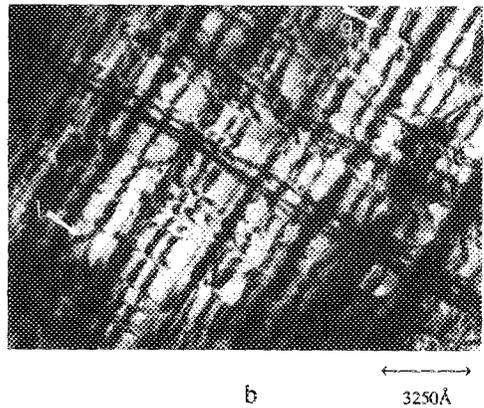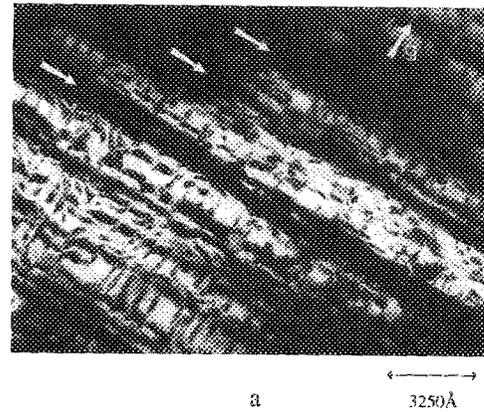
When g is along the dislocation line, most dislocations lose some contrast, and a few disappear, e.g., the dislocation labeled 1 in Fig. 8(b). However, the defects in B always have more contrast than parallel interface dislocations.

Unfortunately, because of the thickness of the sample required for the CL/TEM correlation, g_{040} and g_{400} images were poor, and it was not possible to examine the defects in B under other excitations besides those at the [001] pole. Table I summarizes the TEM observations and classifies the observed contrast into four groups.

The contrast from dislocation type I has already been discussed. These dislocations are edge dislocations and lose contrast entirely when g is along the dislocation line ($g\cdot b = g\cdot b \times u = 0$). These dislocations tend to be located away from the interface and to reside in the GaAs buffer layer. As was shown both in the CL and TEM images where the interface had been removed, the correlation between the images indicates that these dislocations are nonradiative recombination sites.

Type-II dislocations are generally straight and located at the interface. They show contrast for both ⟨220⟩ reflections. They are therefore not edge type. Consider the contrast from a 60°-type dislocation with line direction $u = 1/\sqrt{2}\,[110]$ and $b = 1/2[101]$. Under g_{220} excitation, $g\cdot b = 1$ and $g\cdot b \times u = 0$. Under $g_{2\bar{2}0}$ excitation perpendicular to the dislocation line, $g\cdot b = -1$ and $g\cdot b \times u = \sqrt{2}$.

TABLE I. A summary of defect types observed with TEM in the $In_{0.12}Ga_{0.88}As$/GaAs interface (the dislocation line direction is $[1\bar{1}0]$).

Defect	g_{220} contrast	$g_{2\bar{2}0}$ contrast	Linearity (not at dislocation crossings)	Dark lines in CL of interface
Type I				
1 in Fig. 8(b)	strong	none	wavy, not in interface	no
Type II				
normal interface type	strong	medium	straight	no
Type III				
C	very strong	medium or weak	straight	no
Type IV				
A,B,F,G	very strong	strong	wavy, not in interface	yes

Therefore, for a 60°-type dislocation, one expects good dislocation contrast when g is parallel to u, and stronger contrast when g and u are perpendicular. This is the contrast effect observed for type II, and therefore it is likely that they are 60° dislocations.

Defect type III is composed of dislocations that are straight like type II, but when g is perpendicular to the defect line, stronger contrast than type II is observed. Because of the high dislocation density, their exact nature could not be ascertained. It appears that these defects are composed of groups of dislocations, but do not correspond to dark nonradiative recombination lines.

Finally, type IV is the defect type responsible for the darkest nonradiative recombination lines seen in CL when the interface is present. This type of defect is composed of a group of wavy dislocations located a short distance from the interface. The dislocations do not lose contrast when g is parallel to the dislocation line, and therefore they are not edge dislocations. This type of dislocation exhibits the same contrast features as type II, except the contrast for both $\langle 220 \rangle$ reflections is greater. Type IV is tentatively ascribed to a group of curved 60° dislocations. Because type IV are responsible for high nonradiative recombination, it is tempting to conclude that this is due to the kinks and jogs along the nonlinear group of dislocations.

The reason for the increased contrast of the individual dislocations in the bundle is not known. Two possibilities are that the dislocations are heavily decorated with impurities, or the dislocations have a different Burgers vector. Dislocations with unusually large Burgers vectors, such as $a[100]$ and $a/2[112]$, have been observed in small-angle grain boundaries in Ge by Bourret.[16] The latter dislocation can dissociate into three partials separated by one extrinsic and one intrinsic stacking fault, and Foell and Carter[17] have observed dissociated $a/2[112]$ dislocations in diffusion-bonded Si single crystals. A triple partial of $b = a/2[112]$ could be created in our system by the addition of an edge dislocation and a 60° dislocation. Under our observation conditions, the effective extinction distance is much greater than the partial separation in this defect, so that a dislocation with $b = a/2[112]$ would appear as a single dislocation, and in the correct orientation, it would have the contrast dependence observed for the dislocations in defect B.

D. SEM/CL correlation

Surface ridges on mismatched epitaxial material are frequently observed, but their origin is poorly understood. To investigate the origin of the surface ridges, CL and SEM were obtained from the same area. Figures 9(a) and 9(b) are CL and SEM images, respectively, from the 1-μm $In_{0.12}Ga_{0.88}As$ sample before thinning, i.e., with the epilayer intact. There exists a large asymmetry in the surface ridges, as indicated in Fig. 9(b); one $\langle 110 \rangle$ direction has much more prominent surface ridges. To achieve contrast from the smaller ridges in the other direction, the larger ridges were aligned with the SEM detector. Figure 9 shows that most of the surface ridges seen in SEM correlate with the dark defect lines seen in CL.

To explain this correlation, consider that defects at internal interfaces can affect the epilayer in two ways. First, the dislocations that glide to the interface leave surface steps behind. These steps can act as preferred nucleation sites during epitaxial growth. Second, it has been shown that dislocations with Burgers vectors completely in the interface plane can still act as preferred nucleation sites, presumably because of the compressive and tensile stresses present around the dislocation.[18,19] Therefore, the surface morphology of an epitaxial layer is related to the strain state of the epilayer, which is influenced by defects at the interface. Our results show that dark nonradiative recombination lines correspond to unique dislocation groups with high TEM contrast, presumably because of large stress fields. The stress field associated with these defects can act as a preferred nucleation site for epitaxial growth.

Strain effects from these stress fields are expected to affect the epilayer for thousands of angstroms (a few μm's), depending on the lattice mismatch. Because $In_{0.12}Ga_{0.88}As$ on GaAs has a misfit $\Delta a/a \approx 0.85\%$, a 60° dislocation spacing of ≈ 235 Å is required to totally relax the epilayer. The observed TEM dislocation spacing is 400–1000 Å; therefore, not all of the strain in the epilayer is relieved by dislocations, and elastic strain effects are still present in the epilayer.

Recent elastic strain measurements with the use of ion blocking and x-ray rocking curve techniques[20] confirm the existence of residual strains. The elastic strain left in an InGaAs film grown on GaAs shows a large asymmetry
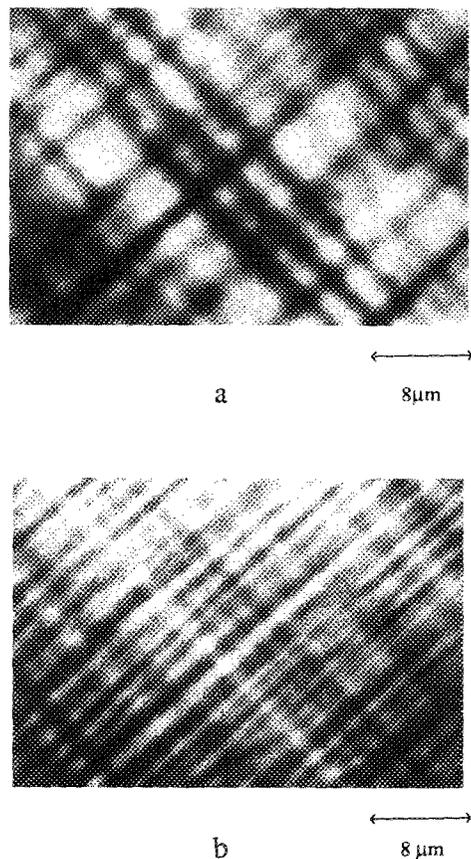
a   ⟵ 8μm ⟶

b   ⟵ 8 μm ⟶

FIG. 9. CL amd SEM images from the same area; (a) CL image; (b) SEM image.

along the two ⟨110⟩ directions,[20,21] presumably because of the different mobilities of the α and β dislocations.[22] The asymmetry of both the surface morphology and elastic strain state of the epilayer also suggest a link between the two.

E. A model for the formation of edge dislocations in the buffer layer

Because dislocations in this crystal system glide to the interface on {111} planes, the most probable dislocation reaction is that described in Eq. (1) [via (2)-(4)], in which two dislocations with different ⟨110⟩ Burgers vectors on the same glide plane react to form an edge dislocation. Evidence that 60° dislocations can loop away from the interface towards the buffer layer has been shown. For loops on the epilayer side of the interface or at the interface, mechanisms such as those described by Hagen and Strunk[23] and Strunk, Hagen, and Bauser[24] could produce edge dislocations. Hagen and Strunk propose an interaction between perpendicular 60°-type dislocations which can produce a node (many can be seen in the TEM micrographs in this paper) and may glide to the surface creating two free-end dislocations. The two new dislocation lines extend through the epilayer; they are free to cross slip and glide to create more misfit dislocations. Two Burgers vectors described in Eq. (1) may then join along their dislocation lines to form an edge dislocation. However, many of the edge dislocations we observed were in the buffer layer, and formation of dislocations in the

buffer layer requires a different mechanism. Dislocation segments extending to the surface from the buffer layer would be inclined to the interface, and their motion would be hindered by the dislocations at the interface. Also, our experimental evidence shows that many of the edge dislocations exist in a broken-line configuration, suggesting that they are a product of a dislocation once lying at the interface along that line. This would agree with the pinned sections seen along the edge dislocation lines, since areas where dislocation reactions occurred could create Burgers vectors that make glide more difficult.

We propose a scenario in which two 60°-type dislocations with appropriate Burgers vectors [see Eq. (1)] are expelled from the interface into the buffer layer, where they combine to form an edge dislocation by the process described in Eqs. (2)-(4). We first note that the Burgers vector of an interfacial 60° dislocation does not lie in the interface plane. The part of the Burgers vector lying in the interface plane will relieve some of the misfit stress. However, the interfacial 60° dislocations have two "extra" components that do not relieve stress in the epilayer: a screw component along the dislocation line and the fraction of the edge component that is perpendicular to the interface. The essential assumption of the model is that the distribution of the 60° dislocations is not ideal, the ideal distribution being that dislocations are arranged such that the extra components mentioned above cancel locally. The ideal distribution is difficult to generate by slip processes, since a dislocation source produces dislocations with identical Burgers vectors. Groups of identical 60° dislocations at the interface relieve misfit strain, but the uncompensated extra components generate a local stress. To avoid a global rotation and tilt (i.e., the formation of a small-angle twist or tilt boundary superimposed on the interface), an equal number of groups with opposing extra components must exist. In this situation, the effectiveness of the in-plane edge component to relieve epilayer stress is not critically dependent on the location respective to the interface. Therefore, the dislocations can deviate into the buffer layer a distance that is a small fraction of the epilayer thickness. If the group spacing is small compared to the epilayer thickness, the energy associated with the accumulated extra components in an individual group can be relieved by expelling a dislocation into the buffer layer.

For a simple model of a dislocation group, consider a small section of the interface array consisting of 60° dislocations, and consider a 60° dislocation in the buffer layer a distance x along a {111} plane from the interface (see Fig. 10). A Peierls' force (F_p), an image force from the interface (F_i), a line tension force (F_i), and a force from the elastic strain from the buffer layer (F_e) act to prevent the dislocation from moving into the buffer layer, and repulsion forces from 60° dislocations with the same Burgers vector (F_d) act to move the dislocation into the substrate. The larger strain in the epilayer prevents the interface dislocations from moving into the epilayer. In this model, the distance x along the {111} plane is determined from the balance of the forces acting on the dislocations
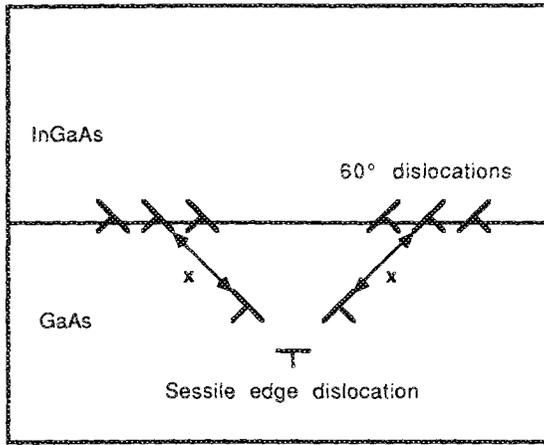
$$F_d = F_e + F_i + F_p + F_l. \tag{5}$$

FIG. 10. Mechanism of producing a sessile edge dislocation in the buffer layer from 60° dislocations with opposite screw components.

Rough calculations of the Peierls' force show that it is small for the growth conditions considered compared to the other forces in Eq. (5), and it will therefore be omitted for these calculations. The glide force per unit length from the elastic strain in the buffer layer is

$$F_e \approx (1/\sqrt{3})b_x Y\epsilon = (a/2\sqrt{3}) Y\epsilon, \tag{6}$$

where Y is the Young's modulus of the buffer layer in the $\langle 100 \rangle$-type direction, b_x is the Burgers vector component in the x direction, ϵ is the strain in the buffer layer, and the $(1/\sqrt{3})$ factor is the fraction of force causing glide for a 60° dislocation with a line direction along $\langle 110 \rangle$ in the interface plane. Considering that the substrate is much thicker than the epilayer, most of the elastic strain should reside in the epilayer. Also, we will assume that no misfit dislocations have yet propagated into the buffer layer. Under these conditions, the elastic strain in the buffer layer is initially near zero, making $F_e = 0$ initially.

Therefore, we are left with the force from the dislocations at the array balancing the image force of the interface and line tension. The force per unit length from the interaction of the buffer layer dislocation with local dislocations of the same Burgers vector at the interface is

$$F_d = \left(\frac{Gb_e^2}{2\pi(1-\nu)}\right) \sum \frac{x(x^2 - y^2)}{(x^2 + y^2)^2}$$

$$+ \left(\frac{Gb_s^2}{2\pi}\right) \sum \frac{x}{(x^2 + y^2)}, \tag{7}$$

where the first term represents the force from the edge component along x, and the second term describes the force from the screw component resolved along x. G is the shear modulus for dislocations in the 60° orientation, b_e and b_s are the edge and screw components of the Burgers vector, the sum Σ is over the dislocations at the interface, and ν is the Poisson's ratio.

The image force per unit length attracting the dislocation back to the interface is approximated by

$$F_i \approx [Gb^2/4\pi(1-\nu)] \left[(1-\nu \cos^2 \alpha)\sin \theta \right]/R, \tag{8}$$

where α is the angle between the dislocation line and the

Burgers vector, θ is the angle between the slip plane and the interface plane, and R is the upper cutoff radius of the dislocation, taken here to be the distance to the interface.

The line tension force per unit length pulling the dislocation segment back to the interface is approximately

$$F_l \approx \beta \left(\frac{Gb^2}{4\pi(1-\nu)}\right) \frac{(1-\nu \cos^2 \alpha)}{\rho} \left[\ln\left(\frac{x \sin \theta}{b}\right) + 2\right], \tag{9}$$

where β is a constant depending on the geometry of the segment, and ρ is the radius of curvature of the segment.

Calculation of Eqs. (7)–(9) for an interface group of five dislocations spaced 250–500 Å apart results in a balanced force position on the order of 1000 Å from the interface, agreeing with our experimental results. A dislocation can rest at this position without experiencing any net force. The image force used in Eq. (8) is an overestimate, and the force expressions used for the image force and line tension become inaccurate when near the interface because of the ambiguity associated with the upper cutoff radius of the dislocation. Despite its simplicity, the model explains the following: (1) The buffer layer can be deformed more easily, since the epilayer side has a much larger elastic strain force; (2) regions of locally high plastic deformation (e.g., groups of misfit dislocations with the same Burgers vectors) in the interface can drive dislocations into the buffer layer to form edge dislocations.

IV. SUMMARY AND CONCLUSIONS

The defect structure of lattice-mismatched $In_{0.12}Ga_{0.88}As$ was analyzed with cathodoluminescence, transmission electron microscopy, high-voltage electron microscopy, and scanning electron microscopy. A HVEM/CL correlation of the same area revealed that the dislocation spacing in the array is 400–1000 Å, but the dark nonradiative recombination line spacing observed in CL is an average of 3 μm. Thus we have observed that the dark nonradiative recombination lines seen in scanning luminescence experiments for this higher misfit system ($\approx 0.85\%$) are not identical to misfit dislocations. The dark nonradiative recombination lines observed in CL coincide with dislocations that deviate slightly from the interface plane and exhibit unusual TEM contrast behavior. SEM and CL images of the same area show that surface ridges correlate with the dark nonradiative recombination lines. It is proposed that the surface reflects the strain state of the epilayer, and misfit defects act as preferred nucleation sites during growth, resulting in a rippled surface. A strong asymmetry in the surface ridges suggests that the elastic strain and nucleation sites from defects are not equivalent along perpendicular $\langle 110 \rangle$ directions. The asymmetry is tentatively attributed to the mobility difference of the α and β dislocations.

TEM cross sections show that the dislocations that deviate from the interface plane lie predominantly on the GaAs buffer layer side of the heterojunction. Step etching and CL show that the buffer layer dislocations are nonradiative recombination centers. Burgers vector analysis determined that the buffer layer dislocations are sessile edge dislocations. Nonradiative recombination at the edge dislocations is attributed to either kinks or a nonreconstructed core consist-

ing of a stair rod and two partial dislocations. A simple model is proposed which describes edge dislocation formation in the buffer layer. The model predicts that as the density of dislocations increases at the interface, dislocations with appropriate Burgers vectors can be expelled into the buffer layer and combine to form an edge dislocation.

ACKNOWLEDGMENTS

[1]T. J. Drummond, W. Kopp, R. Fischer, H. Morkoç, R. E.Thorne, and A. Y. Cho, J. Appl. Phys. 53, 1238 (1982).

[2]R.Fischer, J. T. Drummond, J. Klem, W. Kopp, T. S. Henderson, D. Perrachione, and H. Morkoç, IEEE Trans. Electron Devices ED-31, 1028 (1984).

[3]S. Katsumoto, A. Yamamoto, and M. Yamaguchi, Jpn. J. Appl. Phys. 24, 636 (1985).

[4]J. J. Rosenberg, M. Benlamri, P. D. Kirchner, J. M. Woodall, and G. D. Pettit, IEEE Electron Device Lett. EDL-6, 491 (1985).

[5]H. Ito and T. Ishibashi, Jpn. J. Appl. Phys. 25, L421 (1986).

[6]L. P. Ramberg, P. M. Enquist, Y.-K. Chen, F. E. Najjar, L. F. Eastman, E. A. Fitzgerald, and K. L. Kavanagh, J. Appl. Phys. 61, 1234 (1987).

[7]J. W. Matthews, S. Mader, and T. B. Light, J. Appl. Phys. 41, 3800 (1970).

[8]O. Ueda, I. Umebu, S. Yamakoshi, and T. Kotani, J. Appl. Phys. 53, 2991 (1982).

[9]O. Ueda, K. Wakao, A. Yamaguchi, S. Isozumi, and S. Komiya, J. Appl. Phys. 57, 1523 (1985).

[10]S. Yamakoshi, M. Abe, O. Wada, S. Komiya, and T. Sakurai, IEEE J. Quantum Electron. QE-17, 167 (1981).

[11]P. M. Petroff, R. A. Logan, and A. Savage, J. Microsc. 118, 255 (1980).

[12]J. Marek, R. Geiss, L. Glassman, and M. Scott, J. Electrochem. Soc. 132, 1502 (1985).

[13]B. DeCooman, Ph.D. thesis (Cornell University, Ithaca, NY, 1987).

[14]M. S. Abrahams, L. R. Weisberg, C. J. Buiocchi, and J. Blanc, J. Mater. Sci. 4, 223 (1969).

[15]J. W. Matthews and A. E. Blakeslee, J. Cryst. Growth 27, 118 (1974).

[16]A. Bourret and J. Desseaux, Philos. Mag. 39, 405 (1979).

[17]H. Foell and C. B. Carter, Philos. Mag. 40, 497 (1979).

[18]E. Bauser and H. Strunk, Thin Solid Films 93, 185 (1982).

[19]F. C. Frank, J. Cryst. Growth 51, 367 (1981).

[20]K. L. Kavanagh, P. Maree, and J. C. Barbour (unpublished).

[21]H. Nagai, J. Appl. Phys. 43, 4254 (1972).

[22]J. W. Matthews, J. Vac. Sci. Technol. 12, 126 (1975).

[23]W. Hagen and H. Strunk, Appl. Phys. 17, 86 (1978).

[24]H. Strunk, W. Hagen, and E. Bauser, Appl. Phys. 18, 67 (1979).